3D Frequency-Domain Ultrasound Waveform Tomography Breast Imaging

Gursharan Yash Sandhu[a], Erik West[a], Cuiping Li[a,b], Olivier Roy[a,b], and Neb Duric[a,b];

[a]Delphinus Medical Technologies, USA;

[b]Karmanos Cancer Institute, USA

ABSTRACT

Frequency-domain ultrasound waveform tomography is a promising method for the visualization and characterization of breast disease. It has previously been shown to accurately reconstruct the sound speed distributions of breasts of varying densities. The reconstructed images show detailed morphological and quantitative information that can help differentiate different types of breast disease including benign and malignant lesions. The attenuation properties of an *ex vivo* phantom have also been assessed. However, the reconstruction algorithms assumed a 2D geometry while the actual data acquisition process was not. Although clinically useful sound speed images can be reconstructed assuming this mismatched geometry, artifacts from the reconstruction process exist within the reconstructed images. This is especially true for registration across different modalities and when the 2D assumption is violated. For example, this happens when a patient's breast is rapidly sloping. It is also true for attenuation imaging where energy lost or gained out of the plane gets transformed into artifacts within the image space. In this paper, we will briefly review ultrasound waveform tomography techniques, give motivation for pursuing the 3D method, discuss the 3D reconstruction algorithm, present the results of 3D forward modeling, show the mismatch that is induced by the violation of 3D modeling via numerical simulations, and present a 3D inversion of a numerical phantom.

Keywords: 3D, ultrasound, sound speed, attenuation, waveform tomography, breast cancer, clinical breast imaging, quantitative imaging

1. INTRODUCTION

Ultrasound techniques have been successful in detecting and classifying breast disease.[1] By incorporating the principles of tomography with a ring array ultrasound transducer array, researchers have created the relatively new modality of ultrasound tomography.[2–7] The technique is capable of producing typical B-mode reflection images[8] in addition to quantifying the sound speed and attenuation properties of a breast by using travel-time (ray) based techniques.[9,10] In contrast to travel-time techniques, frequency-domain waveform tomography techniques more accurately model the physics of wave propagation. This has allowed gradient descent inversion algorithms to reconstruct more accurate sound speed distributions of the insonified medium by iteratively minimizing a cost function defined as the difference between real and synthetically generated acoustic pressure fields.[11–17] By allowing the sound speed to have an imaginary part, one is able to model the intrinsic attenuation of a medium.[17,18]

One problem that exists with the image reconstruction process is the assumption of a 2D geometry while the data acquisition process is in 3D. A representation of the data acquisition process is seen in Figure 1a. In the data acquisition process, all ultrasound transducer elements, which lie on the ring array transducer, sequentially emit ultrasound while the other elements record the propagated wave field. To maximize the energy received at the receiving transducers, the beam is focused using a lens. However, as seen in Figure 1b, the beam inherently diverges as it propagates through the medium. Thus, the received signal sampled at the receiver elements

Further author information:

gsandhu@delphinusmt.com

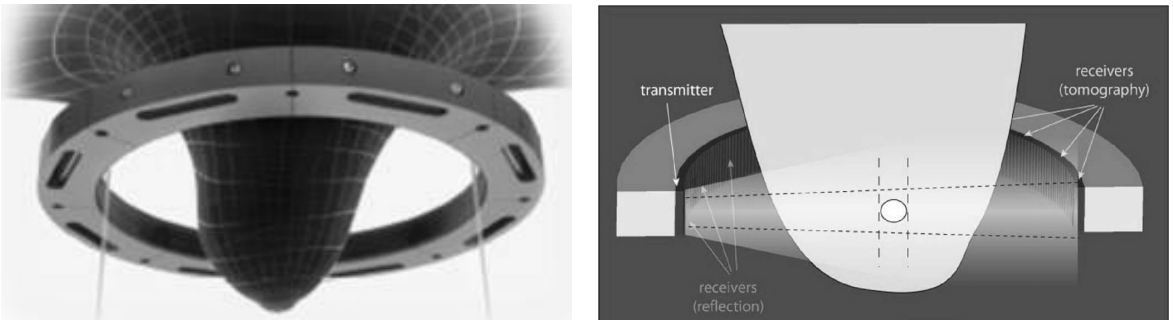

(a) (b)

Figure 1: Ultrasound tomography data acquisition. (a) Scanning procedure; (b) Divergence of focused beam.

represents the kinematics of wave propagation within the acoustic volume defined by the vertical and horizontal contours of the ultrasound wave field and not only in the plane of the transducer ring. Thus, the reconstructed 2D image slice contains the projection of anatomical features which were not in the plane of the transducer ring. This problem leads to several complications in imaging analysis. For example, some problems exist when registering images across different imaging modalities. Assuming a 2D geometry also implies that we do not expect rapid variation along the axis of the imaging ring (z-direction). When this assumption is violated, for example when a breast rapidly slopes or changes shape in the z-direction, artifacts are injected into the reconstructed image. An example of smeared out sound speed halos on the outer edges of 4 different patient breast scans is seen in Figure 2. Test subjects demonstrate a cancer at 10 o'clock, a cancer at 3 o'clock, a very small fibroadenoma in the center of the breast, and many regions of dense parenchyma in Figures 2a, 2b, 2c, and 2d, respectively. Note that the image in Figure 2d also has a very low sound speed cycle skipping streak arching in upper right hand side of the breast from 12 to 3 o'clock. The full stack corresponding to Figure 2d is seen in Figure 7 where one can see another example of a cancer and sound speed smearing on the outer contours of the breast.

The 2D assumption is also a problem for attenuation imaging where any energy lost or gained out of plane is not properly accounted for by the reconstruction algorithm.[19] The reconstruction algorithm compensates by introducing artifacts into the image. For example, in Figure 3, one can see attenuation images (see Section 2) corresponding to two slices of a heterogeneous *ex vivo* phantom containing tumor mimicking lesions of different attenuations and sound speeds. In the images, brighter areas correspond to greater attenuation while darker areas correspond to less attenuation. By comparing Figures 3a and 3b, it is seen that the lesion at 11 o'clock has opposite polarities even though it is of uniform attenuation. The difference is that in one scan, the entire lesion was in the path of the ultrasound beam while in the other scan, the lesion was not completely in the path.

To address current limitations with our imaging methods, namely to compensate for out of plane energy loss when imaging breast attenuation, we propose the use of a 3D frequency-domain waveform tomography algorithm. Researchers in Geophysics have already investigated the use of a 3D waveform tomography algorithms. For example, 3D waveform tomography may be performed either in the time[20,21] or frequency-domain.[20,22–29] Since our existing software architecture is amenable to the frequency-domain approach, we chose a frequency-domain method,[24] but with a direct LU factorization solver.[11] This is in contrast to many Geophysical applications which use an iterative or hybrid solver to reduce memory and computation expense.[22,23,29] Other methods to reduce computation time include using phase encoding.[28] 3D waveform inversion has also been applied to real data with improved imaging results.[22,26,27] Based on their results and our own hypothesis, we predict that with a 3D algorithm, artifacts near the outer contours of the breasts in Figure 2 as well as cycle skipping streaks should be reduced and the polarity of the lesion in the phantom in Figure 3 should be uniform throughout the image stack. In addition, one would be able to reconstruct an entire breast volume instead of only one slice at a time.

In the following sections, we will review the waveform tomography method including the forward modeling and inversion processes. We will show the results of numerical forward modeling by displaying the resultant 3D pressure fields propagated on a constant sound speed and attenuation medium. We will then compare them to the analytical solutions. In order to to utilize the 3D method on *in vivo* data, an appropriate modeling of the

transducer array beam response must be done. We will show some preliminary work regarding apodizing the beam to focus it in-plane as is done with our ultrasound tomography device. By utilizing a 2D inversion of a breast scan stack, we show the complex wave field generated in 3D. Using 2D inversion on a numerical model, we will show the consequences of assuming a 2D geometry when wave propagation is performed in 3D. We will also show a numerical reconstruction when both forward modeling and inversion is done on a 3D numerical model.

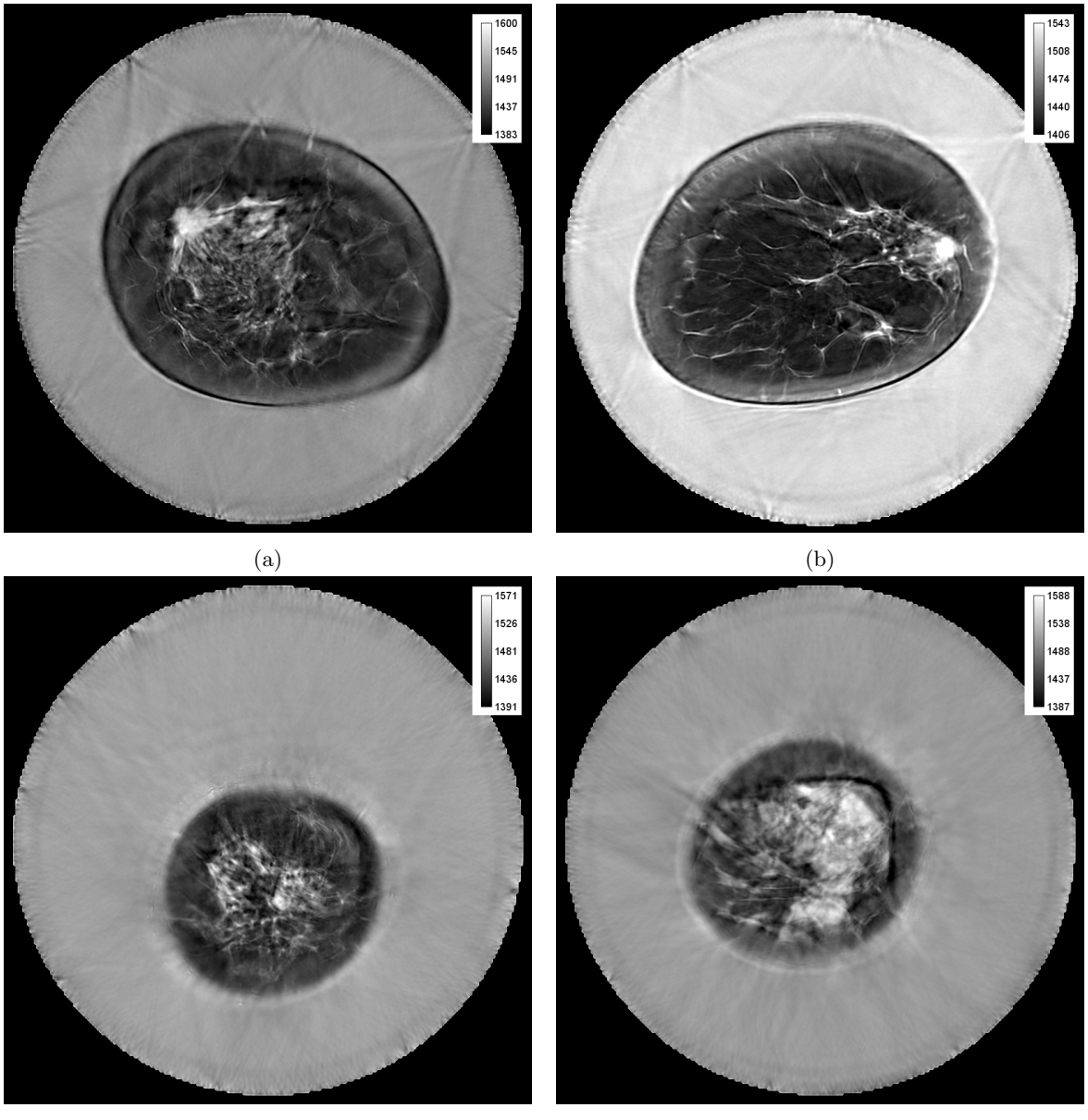

(a) (b)

(c) (d)

Figure 2: Examples of 3D sound speed smearing artifacts arising on the outer contours of the breast. Calibration bars are in units of m/s. (a) Sound speed image with cancer at 10 o'clock; (b) Sound speed image with cancer at 3 o'clock. (c) Sound speed image with fibroadenoma at center. (d) Sound speed image with dense parenchyma. A cycle skipping streak in the upper right hand side of the image from 12 to 3 o'clock is also visible.

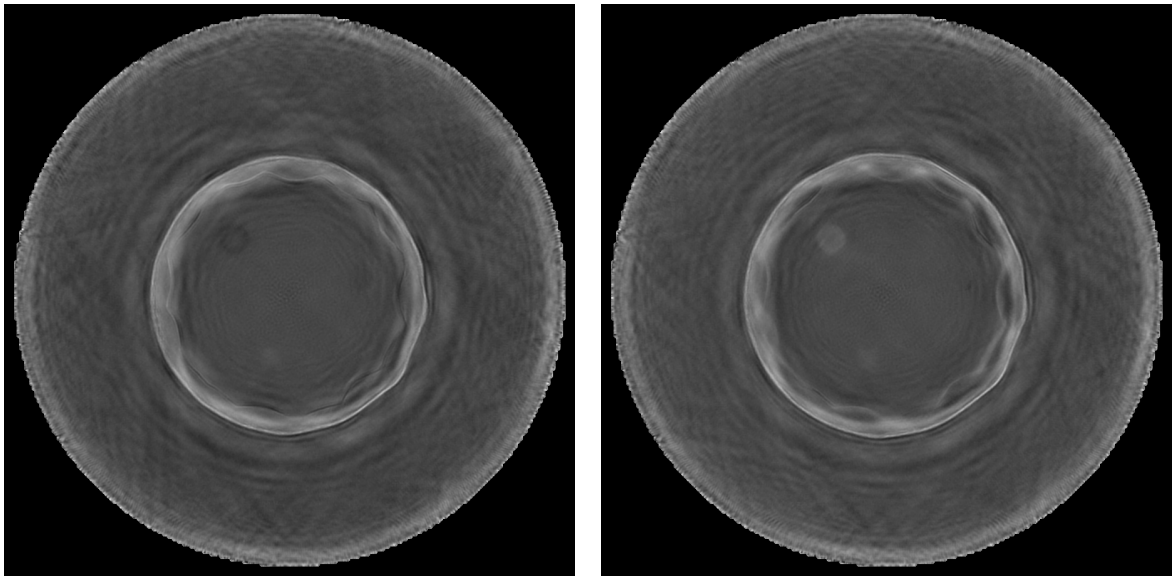

(a) (b)

Figure 3: Attenuation images of *ex vivo* heterogeneous breast phantom. (a) Attenuation image of slice 7; (a) Attenuation image of slice 10.

2. METHOD

2.1 Theory

Using finite difference methods,[24] we solve the 3D Helmholtz equation to obtain a pressure field $\mathbf{u}$ for a given source $\boldsymbol{\delta}$, frequency $\omega = 2\pi f$, and complex valued sound speed $\mathbf{c}$

$$\left(\nabla^2 + \frac{\omega^2}{c^2}\right)\mathbf{u}(\omega, \mathbf{c}) = -\boldsymbol{\delta}(\omega)\,. \tag{1}$$

Initially, Equation 1 is solved using an initial guess $\mathbf{c} = \mathbf{c}_0$ to the true sound speed $\mathbf{c}_{true}$ of the object that is imaged. The resulting wave field $\mathbf{u}$ is then compared to the observed wave field $\mathbf{d}_{obs}$. For numerical simulations, $\mathbf{d}_{obs}$ is obtained by solving the Helmholtz equation using $\mathbf{c}_{true}$ and sampling on grid points corresponding to the ultrasound ring transducer array. For real life applications, the wave field $\mathbf{d}_{obs}$ is created and obtained by propagating ultrasound using our ring array transducer device and sampling the received wave forms. Using the sampled numerical wave field on the transducer array $\mathbf{u}_{obs}$ and $\mathbf{d}_{obs}$, a cost function E is created

$$E(\omega, \mathbf{c}) = \frac{1}{2}\,\mathbf{e}^H(\omega, \mathbf{c})\,\mathbf{e}(\omega, \mathbf{c})\,,$$

where ^{H} denotes the Hermitian transpose and $\mathbf{e}$ is the residual mismatch defined as

$$\mathbf{e}(\omega, \mathbf{c}) = \mathbf{u}_{obs}(\omega, \mathbf{c}) - \mathbf{d}_{obs}(\omega, \mathbf{c}_{true})\,.$$

We then iteratively update the sound as given by

$$\mathbf{c}^{(i+1)} = \mathbf{c}^{(i)} - \alpha \nabla E(\omega, \mathbf{c}^{(i)})\,,$$

where the step size α is determined by line search[30] or a linear estimate,[31] and the cost function gradient $\nabla E = \partial E/\partial c$ is taken with respect to the real (c_R) or imaginary (c_I) part of the complex valued sound speed. An effective matrix formulation[11] of Equation 1 is given by

$$A\mathbf{u} = \boldsymbol{\delta}\,,$$

where A represents the Helmholtz operator. The cost function gradient is then given by

$$\nabla E = \mathrm{Re}\left\{ \mathbf{u}^H \left(-\frac{\partial A}{\partial c} \right)^H (A^{-1})^H \mathbf{e} \right\}, \tag{2}$$

where Re{ } indicates taking the real part of the expression in parenthesis. To model attenuation, we give a non-zero imaginary sound speed c_I whose relation to an attenuation coefficeint α is given by

$$\alpha = -\frac{20}{\ln 10} \frac{2\pi c_I}{c_R^2}.$$

Regarding units, if $[c] = [\mathrm{km/s}]$, then $[\alpha] = [\mathrm{dB/mmMHz}]$. Further details about the data acquisition and reconstruction process can be found in our previous publications.[13–15,17]

2.2 Experiments

A 3D waveform tomography algorithm is a natural extension of the 2D case. Instead of restricting wave propagation to a plane, any type of volume can be used. In particular, we will use a rectangular volume that encompasses the ring transducer array with some height Δz above and below the center position of the transducer ring. Due to computation cost, decisions we have made in our software architecture, and the current limitations of computing hardware, we are limited in either the maximum size of the computational domain or the highest achievable frequency. Namely, the computation domain must be large enough in every dimension such that there is sufficient room for wave propagation and PML damping. In order to model the frequency content of our ultrasound transducer array, we reduce the radius of the transducer ring. Likewise, we could keep the radius and reduce the modeled frequency. For numerical simulation, this is not a hindrance. Images were displayed and processed using ImageJ[32] and Matlab.[33] Algorithms were developed using C/C++/CUDA and were run on a workstation with 256 GB RAM, a 14-core 3.2 GHz Intel Xeon E5-2696 v3 processor, and a 12 GB RAM NVIDIA TITAN X GPU. However, the LU factorization and subsequent forward and backwards substitutions, where the overwhelmingly vast majority of computation cost resides, were done only using a single-threaded CPU implementation.

2.2.1 Forward Modeling

In the following section, we will first demonstrate the results of numerical forward modeling and its comparison to the analytical solution. We will also show the corresponding wave fields with a non-zero attenuation. We will demonstrate a simple z-direction apodization of the transducer to generate a beam focused in the plane of the transducer array. By using 2D waveform inversion, we create a stack of sound speed images of the breast. This sound speed volume is then used as a sound speed model for 3D wave propagation. The resultant wave field gives an illustration of the wave interactions that are generated in an actual breast.

2.2.2 2D Inversion

We forward propagate in 3D on a true sound speed model consisting of a constant sound speed cylinder embedded in a different constant sound speed medium. We do the same for 2D forward propagation[34] but use a circular disc. Both resulting observed wave fields are then input into our 2D full wave inversion algorithm. The difference between the results, i.e. whether $\mathbf{d}_{obs}$ was generated in 2D or 3D, gives an example of the mismatch and artifact generation that could possibly result in the assumption of a 2D geometry for waveform inversion. Note for this experiment, only the center slice of the 3D wave field was sampled to create $\mathbf{d}_{obs}$ which was used as input to the 2D inversion.

2.2.3 3D Inversion

By using a 3D inversion method, we will show the numerical reconstruction of the 3D forward propagated data of a cylinder. As was the case for the 2D inversion of 3D forward propagated data, $\mathbf{d}_{obs}$ was created only using the center slice.

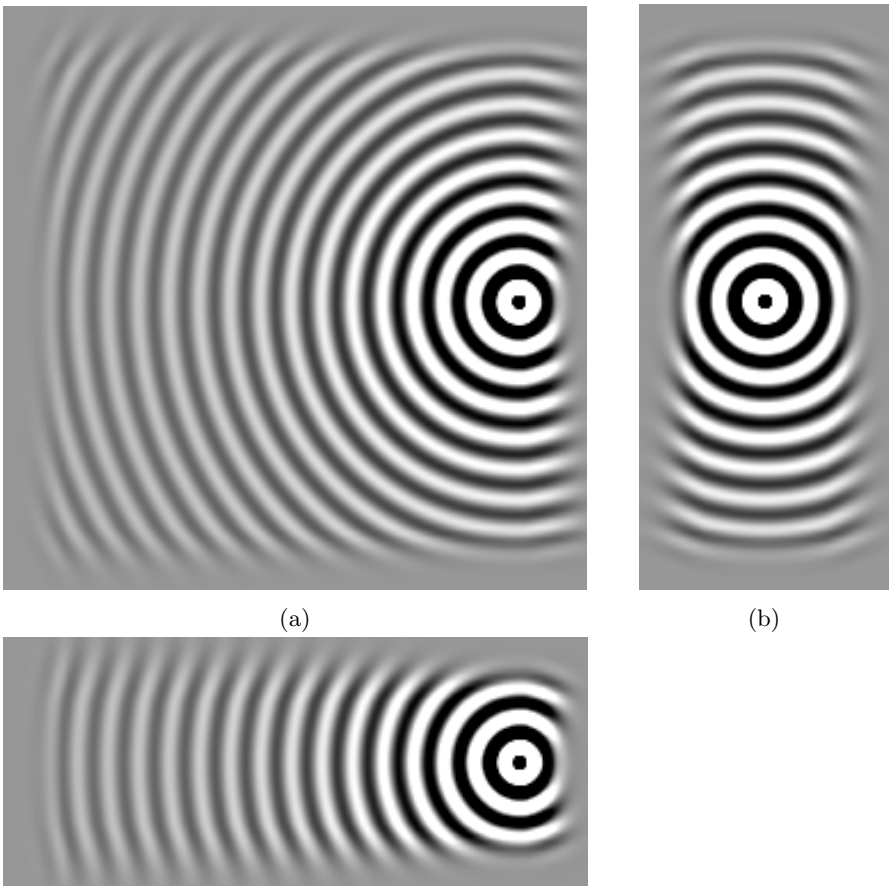

(a) (b)

(c)

Figure 4: Real part of 100 kHz pressure field generated in a constant sound speed medium. (a) XY Plane; (b) YZ Plane; (c) XZ Plane.

3. RESULTS

3.1 Forward Modeling

The real part of the resulting pressure field $\mathbf{u}$ after solving Equation 1 is shown in Figure 4. Modeling was done on a constant sound speed of $c = 1500$ m/s, frequency $f = 200$ kHz, wavelength $\lambda = c/f$, and cosine perfectly matched layers (PML) of length 2λ in a medium of size $144 \times 144 \times 61.5$ mm ($\hat{\mathbf{x}} \times \hat{\mathbf{y}} \times \hat{\mathbf{z}}$) corresponding to $96 \times 96 \times 41$ pixels with a grid discretization of $\lambda/5 = 1.5$ mm. The source location corresponds to a grid index on a circular transducer ring with a reduced radius of 55 mm. The PML parameters were heuristically chosen to eliminate reflections from the boundary of the numerical domain. It can be seen that the wave fields are very smooth without reflections. The wave fields decay rapidly once they reach the PML. In Figure 5, we compare the wave fields in Figures 4a and 4c to their analytical solutions by creating profiles by sampling on a line within the image and plotting the analytical solution $\exp[ikr]/r$, where $k = \omega/c$ is the wave number, $i = \sqrt{-1}$, and r is the propagation distance. Note that for Figures 5e and 5f, a constant attenuation of 1.0 dB/mmMHz is present in the medium. By examining the different profiles in Figure 5, it can be seen there is an excellent agreement between the analytical and numerical solutions across the entire volume. Note that for the cases without attenuation, once the waves enter the PML, they rapidly decay and thus no longer match the analytical solution.

In order to apply 3D waveform tomography to real ultrasound data, the transducer array must be modeled. A preliminary attempt at modeling the beam was achieved by using a line source with the same unit impulse in each pixel. The line source consists of 13 pixels corresponding to a transducer beam height of 20 mm. A

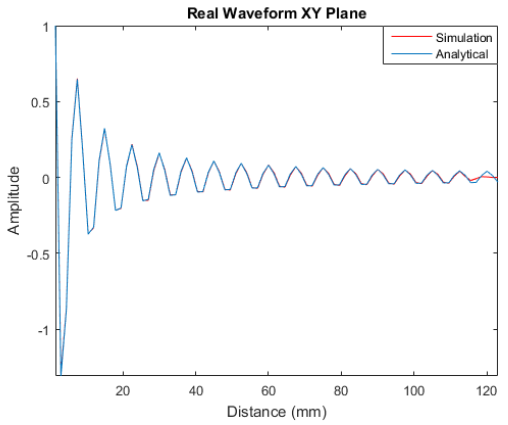

(a)

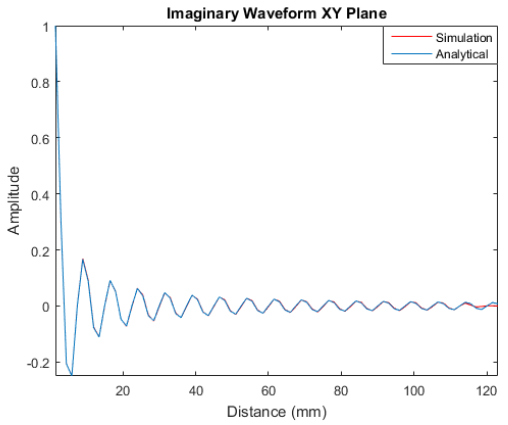

(b)

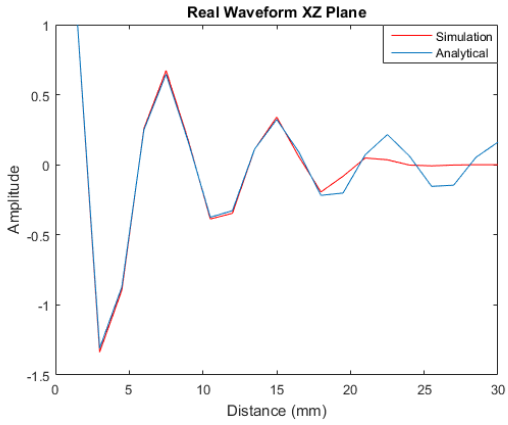

(c)

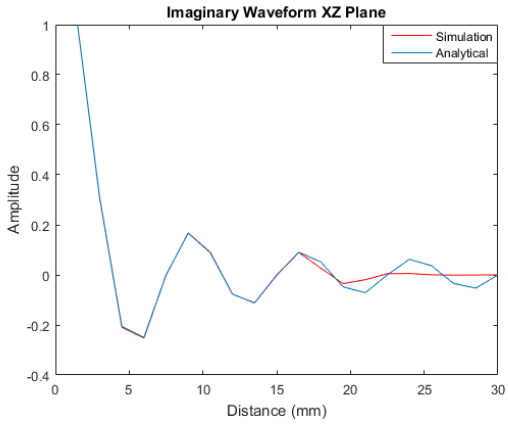

(d)

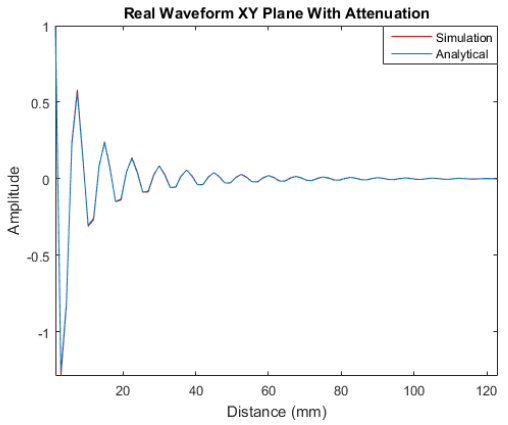

(e)

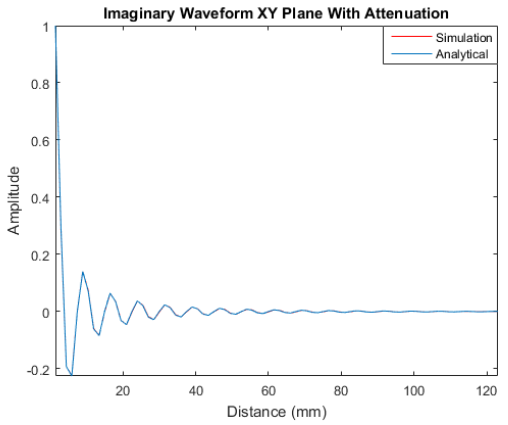

(f)

Figure 5: Comparison of numerical and analytical solutions. (a) Profile of real part of waveform in the XY plane; (b) Profile of imaginary part of waveform in the XY plane; (c) Profile of real part of waveform in the XZ plane; (d) Profile of imaginary part of waveform in the XZ plane; (e) Profile of real part of waveform in the XY plane with attenuation; (f) Profile of imaginary part of waveform in the XY plane with attenuation.

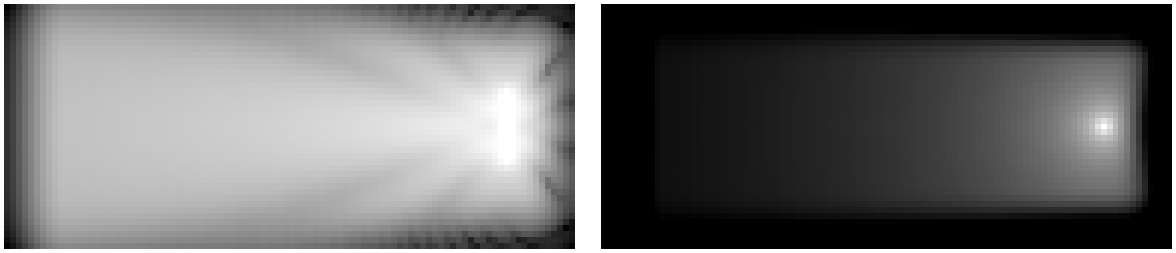

(a) (b)

Figure 6: Comparison of $\log_{10}$ of magnitude of beam profiles in XZ plane. Correspondence of energy intensity and gray scale is consistent in both images. (a) 20 mm line source; (b) Point source.

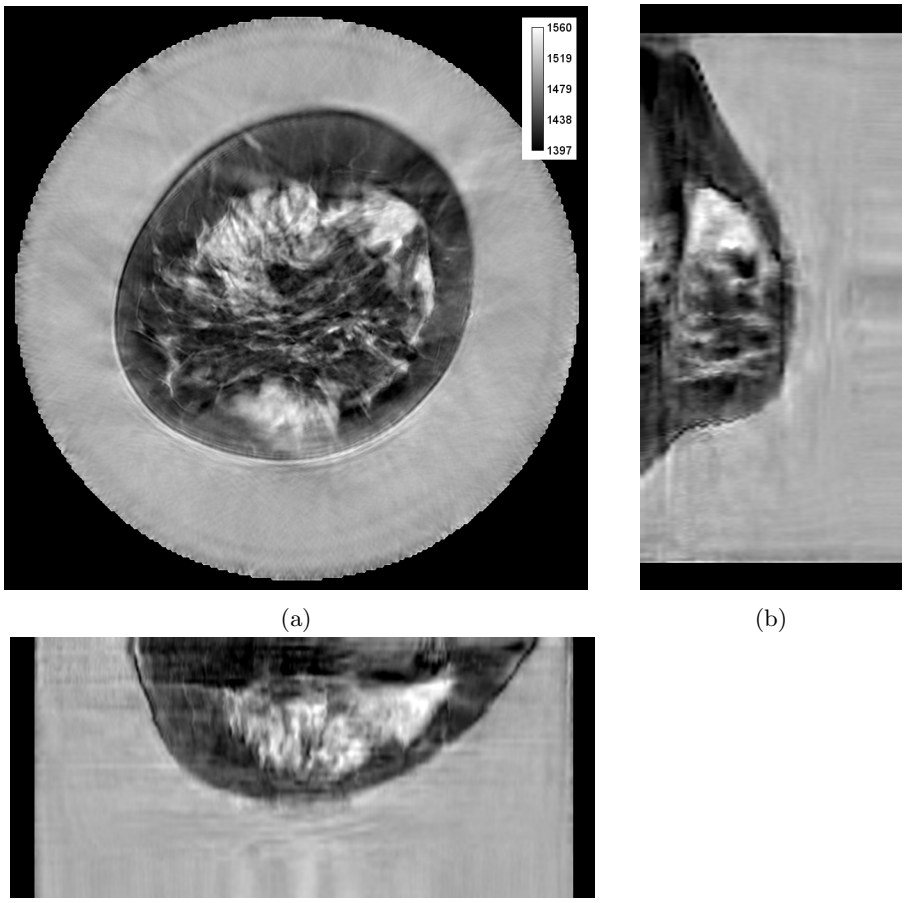

(a) (b)

(c)

Figure 7: 2D inversion sound speed image of breast with cancer. Multi-plane projections intersect at the center of the tumor. Images represent a domain of size $228 \times 228 \times 123$ mm. (a) Coronal plane with cancer at 2 o'clock; (b) Sagittal plane; (c) Transverse plane.

comparison of the $\log_{10}$ of the magnitude of the beam profile in the XZ plane for a point source and the line source is given in Figure 6. The gray scale intensity corresponds to the same energy intensity in both images.

In Figure 7, we see an image of a breast with cancer. The sagittal and transverse projections are also shown. In particular, the projections are centered at the center of the cancer. This breast corresponds to the same patient in Figure 2d. For the wave propagation experiment, the breast stack was resampled and padded such that the grid size of each voxel was 3 mm. This corresponds to $\lambda/5$ at 100 kHz. By doing this, the entire breast volume can be imaged at once. The results of 100 kHz wave propagation on this model is shown in Figure 8. A

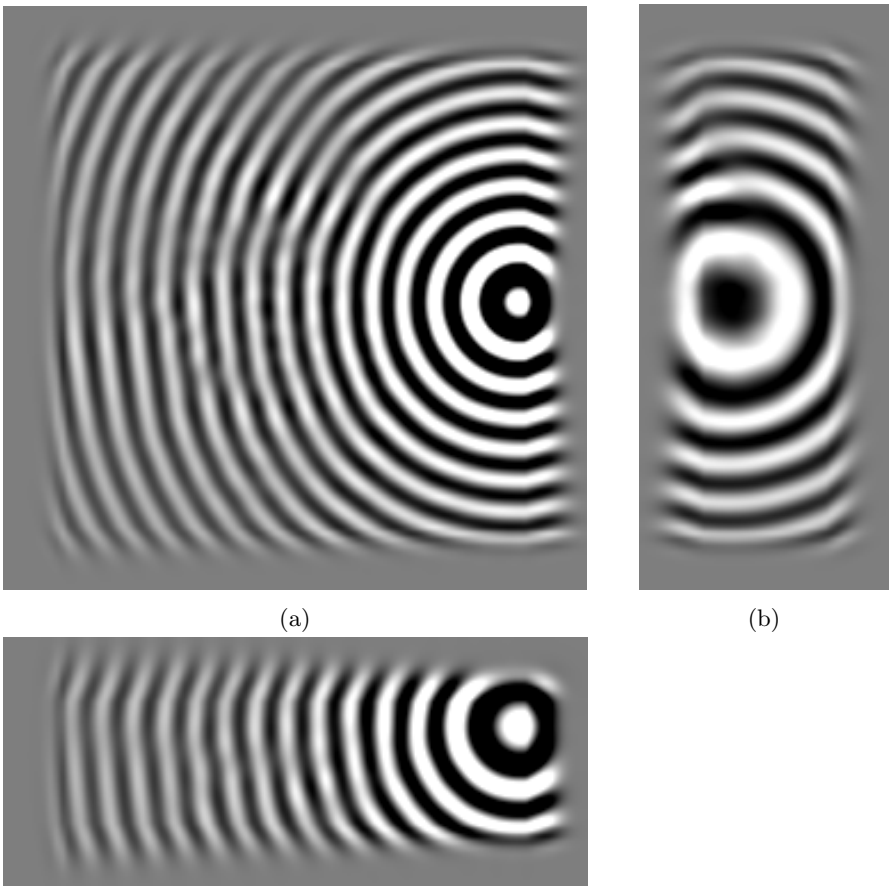

(a) (b)

(c)

Figure 8: Real part of 100 kHz pressure field generated in the breast sound speed stack in Figure 7. Multi-plane projections intersect at the center of the tumor. Images represent a domain of size $288 \times 288 \times 123$ mm. (a) XY Plane; (b) YZ Plane; (c) XZ Plane.

point source was used on a grid location corresponding to the transducer ring. The z location of the point source corresponded to a voxel in the center of the breast.

3.2 2D Inversion

Using the same parameters as defined in Section 3.1, we perform 3D forward propagation on a cylinder with height 31.5 mm and radius 16.5 mm and a sound speed 1.54 km/s in a background. It is offset from the origin by 6.5 mm in both the x and y-directions. We perform 2D wave propagation on the corresponding disc. The true model is given in Figure 9. Using the data sampled on the middle slice of the cylinder, the corresponding 2D inversion using an amplitude normalized phase only cost function is seen in Figure 10a. The 2D inversion of a disc using 2D forward propagated data using a amplitude normalized phase cost function and normal cost function is shown in Figures 10b and 10c, respectively. For the inversion, 10 iterations were done at 200 kHz. The starting model was a constant 1.5 km/s medium. Note that our 2D wave simulator yields solutions with phase $\exp[-ikr]$ while the 3D wave simulator has solutions with phase $\exp[ikr]$. Thus, the conjugate of the 3D pressure field was needed before 2D inversion. Also, the mismatch between geometric spreading, $1/r$ for 3D and $1/\sqrt{r}$ for 2D, led to a failed reconstruction. We had to normalize the pressure fields by their magnitude in order to reconstruct the 3D forward propagated data. An example with no amplitude normalization is shown to display the sound speed information lost when amplitude information is lost.

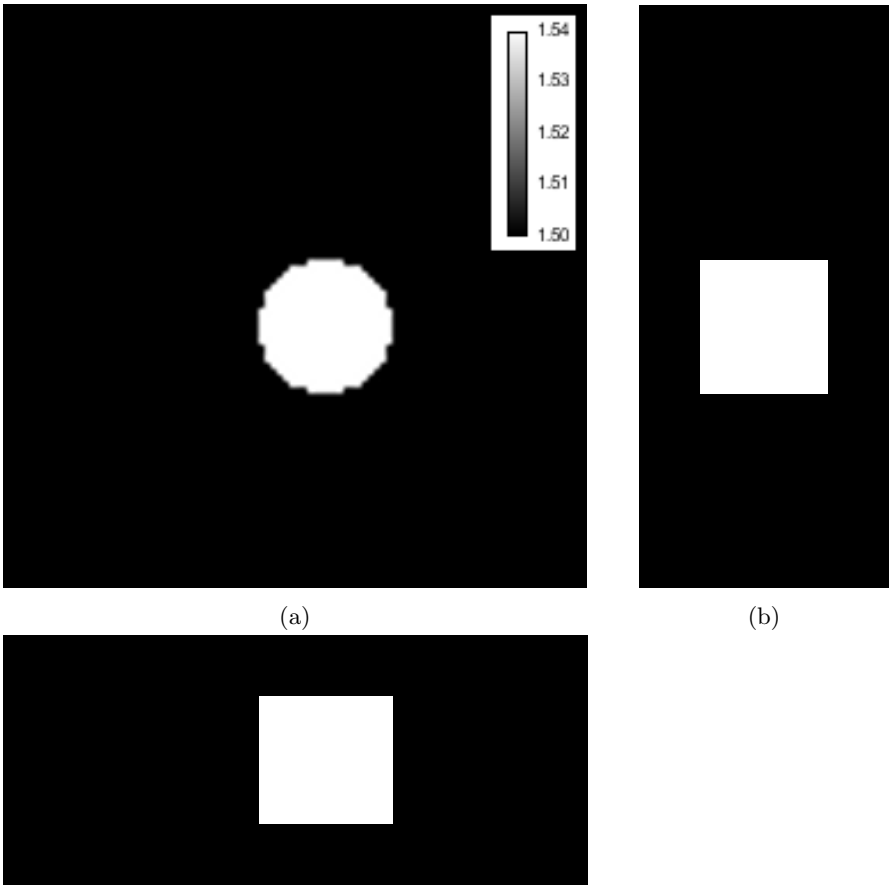

(a) (b)

(c)

Figure 9: Cylinder model used for wave propagation. The height of the cylinder is 31.5 mm and the radius is 16.5 mm. It is offset from the center by 6.5 mm in both the x and y-directions. The sound speed is 1.54 km/s for the cylinder and 1.5 km/s for the background. Disc model is the same as in (a). (a) XY Plane; (b) YZ Plane; (c) XZ Plane.

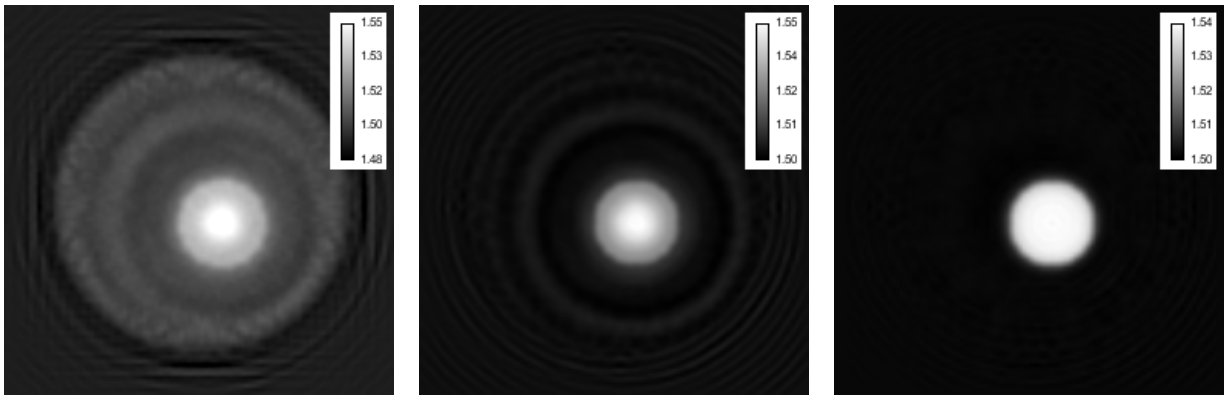

(a) (b) (c)

Figure 10: Reconstructions using a 2D inversion. Calibration bars are in units of km/s. (a) 2D normalized cost function inversion of 3D forward propagated data on a cylinder; (b) 2D normalized cost function inversion of 2D forward propagated data on a disc. (c) 2D normal cost function inversion of 2D forward propagated data on a disc.

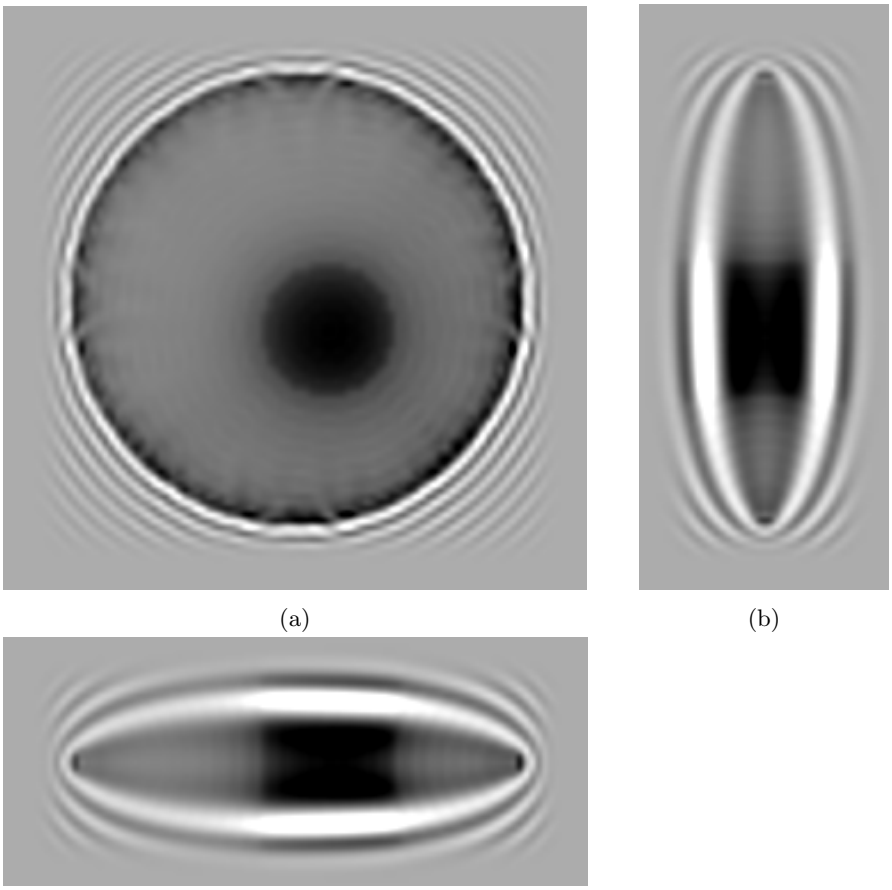

(a) (b)

(c)

Figure 11: 3D gradient image. (a) XY Plane; (b) YZ Plane; (c) XZ Plane.

3.3 3D Inversion

3D wave propagation was done on a cylinder as in Section 3.2. However, the data was inverted using a 3D inversion algorithm. The inversion started with a constant sound speed medium of 1.5 km/s. Ten iterations were done at 200 kHz. The gradient, i.e. Equation 2, for the very first iteration of the inversion is given in Figure 11. The final reconstructed sound speed model is shown in Figure 12.

4. CONCLUSIONS

From the results of numerical forward modeling in 3D, we see that there is an excellent agreement between 3D simulated wave fields and the corresponding analytical solutions. This was also the case when a non-zero attenuation was used. By implementing a simple apodization, we see that the transducer array response becomes more focused in-plane which mimics our transducer ring. By 3D forward modeling on a sound speed breast stack, we see an example of 3D wave interactions in a breast. The wave field is significantly perturbed compared to the example of wave propagation on a constant medium. Ignoring these wave interactions would result in the injection of artifacts into a reconstructed image. The whole breast 3D forward modeling also proves that it would be possible to reconstruct the entire breast volume at once. However, the wave propagation was done at 100 kHz which would lead to a reduction in the contrast and resolution of our sound speed images which are currently iterated to a high enough frequency which allows for us to obtain sub-millimeter resolution. But, it would lead to an improved attenuation reconstruction as we hypothesize out of plane energy loss is currently a limitation of our attenuation reconstructions.

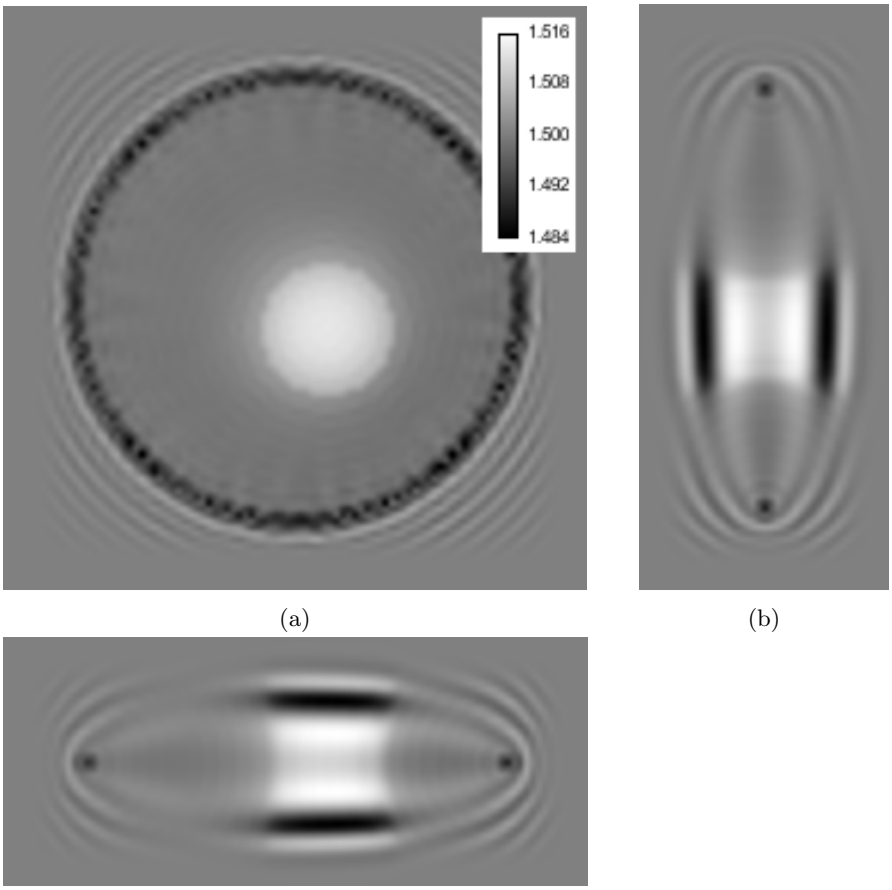

(a) (b)

(c)

Figure 12: 3D sound speed reconstruction. (a) XY Plane; (b) YZ Plane; (c) XZ Plane.

By comparing the results of 2D inversion on data which was generated by using both 2D and 3D forward modeling, we see an example of the possible artifacts that are generated when an incorrect geometry of wave propagation is assumed. Namely, a halo of false sound speed mimicking what is seen in our *in vivo* sound speed images is generated. We do note that an amplitude normalized cost function had to be used to in order to perform this experiment which leads to a reduction in image quality. Normalizing the 3D data with respect to 2D geometric spreading should circumvent the use of a normalized cost function. An ideal source apodization that could model a transducer's beam response in 3D would also be able to be used in a 2D inversion resulting in similar artifacts to our *in vivo* images.

From observing the gradient image, it can be seen that the 3D algorithm is updating voxels corresponding to the location of the cylinder. In particular, the cylinder dimensions is such that its height is 4λ at 200 kHz. The PML needs 2λ for each layer. Thus, the PML straddles the edge of the cylinder. This could potentially create problems with the reconstruction, However, another cause for the inability to resolve the top and bottom layers of the cylinder is due to finite sampling in the z-direction. The reconstructed volume is limited by the width of the 1st Fresnel zone. At 200 kHz and a radius of 55 mm, this would be 14.3 mm which is consistent with the wave path in the gradient image. Thus, the 3D sound speed reconstruction will not be able to resolve the bottom and top layers of the cylinder. This can easily be remedied by using multiple slices of measurements instead of only the central slice. After 10 iterations and only one slice of data, the sound speed reconstruction has yet to converge to the true model. For example, the average sound speed of the cylindrical volume is 1.514 km/s instead of 1.540 km/s. However, the convergence is going in the correct direction and has not diverged. A possible reason for its poor convergence behavior may be due to ignoring scaling ambiguities when converting our implementation of the linear step size estimation for the 3D inversion. Line search was not attempted, but

will be tested to see any improvement in convergence behavior. It is also possible that the solution has not converged yet and simply needs more iterations. The choice of starting model might also be the problem. Using multiple slices of data should also improve convergence behavior. For example, the direct analogy of a circular array in 2D would be a spherical array in 3D. Multiple slices of circular array data should be just as effective.

The biggest hurdle for our 3D algorithm is computational cost and the limitations of current computing hardware. For example, GPU cards do not currently have enough memory to handle the vast memory requirements of 3D wave propagation on meaningful mesh sizes and frequencies. Thus, a single-threaded CPU algorithm was implemented using our existing software architecture and matrix solving method. As a first step, the implementation can be multi-threaded to reduce the time cost. However, the greatest computational expense is generated in the LU factorization. One benefit of the LU factorization approach is the rapid solution of multiple sources. The ratio of time spent in LU factorization and forward/backward substitution of different sources is even higher for 3D when compared to 2D. In this manuscript, only one slice of sources was used. However, the entire cylindrical volume of sources could be used with a very marginal increase in overall time when compared to only a single slice of data. Iterative and hybrid matrix solutions compounded with other algebraic techniques and CPU clusters is the choice for Geophysics applications of 3D waveform tomography. Adopting such techniques or improving our current techniques could possibly make 3D waveform tomography viable in a clinical setting given current computing hardware. If the beam profile of the transducer beam can be properly simulated, regardless of the method used to generate wave fields, improvements in computing hardware will eventually lead to the adoption of 3D waveform tomography techniques.

5. ACKNOWLEDGMENT

This work was partially funded by the National Institutes of Health (NIH) through National Cancer Institute grants R43CA171601 and R44CA165320.

REFERENCES

[1] Stavros, A. T., Thickman, D., Rapp, C. L., Dennis, M. A., Parker, S. H., and Sisney, G. A., "Solid breast nodules: use of sonography to distinguish between benign and malignant lesions.," *Radiology* **196**(1), 123–134 (1995).

[2] Carson, P. L., Meyer, C. R., Scherzinger, A. L., and Oughton, T. V., "Breast imaging in coronal planes with simultaneous pulse echo and transmission ultrasound," *Science* **214**(4525), 1141–1143 (1981).

[3] Duric, N., Littrup, P., Poulo, L., Babkin, A., Pevzner, R., Holsapple, E., Rama, O., and Glide, C., "Detection of breast cancer with ultrasound tomography: First results with the computed ultrasound risk evaluation (CURE) prototype," *Medical physics* **34**(2), 773–785 (2007).

[4] Duric, N., Littrup, P., Schmidt, S., Li, C., Roy, O., Bey-Knight, L., Janer, R., Kunz, D., Chen, X., Goll, J., et al., "Breast imaging with the softvue imaging system: First results," in [*SPIE Medical Imaging*], 86750K–86750K, International Society for Optics and Photonics (2013).

[5] Marmarelis, V. Z., Kim, T.-S., and Shehada, R. E., "High-resolution ultrasound transmission tomography," in [*Medical Imaging 2003*], 33–40, International Society for Optics and Photonics (2003).

[6] Ruiter, N. V., Göbel, G., Berger, L., Zapf, M., and Gemmeke, H., "Realization of an optimized 3d usct," in [*SPIE Medical Imaging*], 796805–796805, International Society for Optics and Photonics (2011).

[7] Wiskin, J., Borup, D., Johnson, S., Berggren, M., Abbott, T., and Hanover, R., "Full-wave, non-linear, inverse scattering," in [*Acoustical Imaging*], 183–193, Springer (2007).

[8] Schmidt, S., Duric, N., Li, C., Roy, O., and Huang, Z.-F., "Modification of Kirchhoff migration with variable sound speed and attenuation for acoustic imaging of media and application to tomographic imaging of the breast," *Medical physics* **38**(2), 998–1007 (2011).

[9] Li, C., Duric, N., and Huang, L., "Clinical breast imaging using sound-speed reconstructions of ultrasound tomography data," in [*Medical Imaging*], 692009–692009, International Society for Optics and Photonics (2008).

[10] Li, C., Duric, N., and Huang, L., "Comparison of ultrasound attenuation tomography methods for breast imaging," in [*Medical Imaging*], 692015–692015, International Society for Optics and Photonics (2008).

[11] Pratt, R. G., "Seismic waveform inversion in the frequency domain, part 1: Theory and verification in a physical scale model," *Geophysics* **64**(3), 888–901 (1999).
[12] Pratt, R. G., Huang, L., Duric, N., and Littrup, P., "Sound-speed and attenuation imaging of breast tissue using waveform tomography of transmission ultrasound data," in [*Medical Imaging*], 65104S–65104S, International Society for Optics and Photonics (2007).
[13] Li, C., Sandhu, G. S., Roy, O., Duric, N., Allada, V., and Schmidt, S., "Toward a practical ultrasound waveform tomography algorithm for improving breast imaging," in [*SPIE Medical Imaging*], 90401P–90401P, International Society for Optics and Photonics (2014).
[14] Sandhu, G. Y., Li, C., Roy, O., Schmidt, S., and Duric, N., "High-resolution quantitative whole-breast ultrasound: in vivo application using frequency-domain waveform tomography," in [*SPIE Medical Imaging*], 94190D–94190D, International Society for Optics and Photonics (2015).
[15] Sandhu, G., Li, C., Roy, O., Schmidt, S., and Duric, N., "Frequency domain ultrasound waveform tomography: breast imaging using a ring transducer," *Physics in medicine and biology* **60**(14), 5381 (2015).
[16] Sandhu, G. S., "PhD thesis: Frequency domain ultrasound waveform tomography breast imaging," (2015).
[17] Sandhu, G. Y. S., Li, C., Roy, O., West, E., Montgomery, K., Boone, M., and Duric, N., "Frequency-domain ultrasound waveform tomography breast attenuation imaging," in [*SPIE Medical Imaging*], 97900C–97900C, International Society for Optics and Photonics (2016).
[18] Aki, K. and Richards, P. G., [*Quantitative seismology*], vol. 1 (2002).
[19] Hooi, F. M., Kripfgans, O., and Carson, P. L., "Acoustic attenuation imaging of tissue bulk properties with a priori information," *The Journal of the Acoustical Society of America* **140**(3), 2113–2122 (2016).
[20] Sirgue, L., Etgen, J., and Albertin, U., "3d frequency domain waveform inversion using time domain finite difference methods," in [*70th EAGE Conference and Exhibition incorporating SPE EUROPEC 2008*], (2008).
[21] Vigh, D. and Starr, E. W., "Comparisons for waveform inversion, time domain or frequency domain?," in [*SEG Technical Program Expanded Abstracts 2008*], 1890–1894, Society of Exploration Geophysicists (2008).
[22] Plessix, R.-É., "Three-dimensional frequency-domain full-waveform inversion with an iterative solver," *Geophysics* **74**(6), WCC149–WCC157 (2009).
[23] Ben-Hadj-Ali, H., Operto, S., Virieux, J., and Sourbier, F., "3d frequency-domain full-waveform tomography based on a domain decomposition forward problem," in [*SEG Technical Program Expanded Abstracts 2008*], 1945–1949, Society of Exploration Geophysicists (2008).
[24] Operto, S., Virieux, J., Amestoy, P., LExcellent, J.-Y., Giraud, L., and Ali, H. B. H., "3d finite-difference frequency-domain modeling of visco-acoustic wave propagation using a massively parallel direct solver: A feasibility study," *Geophysics* **72**(5), SM195–SM211 (2007).
[25] Ben-Hadj-Ali, H., Operto, S., and Virieux, J., "Velocity model building by 3d frequency-domain, full-waveform inversion of wide-aperture seismic data," *Geophysics* **73**(5), VE101–VE117 (2008).
[26] Warner, M., Stekl, I., and Umpleby, A., "3d wavefield tomography: synthetic and field data examples," in [*SEG Technical Program Expanded Abstracts 2008*], 3330–3334, Society of Exploration Geophysicists (2008).
[27] Vigh, D. and Starr, E. W., "3d prestack plane-wave, full-waveform inversion," *Geophysics* **73**(5), VE135–VE144 (2008).
[28] Ben-Hadj-Ali, H., Operto, S., and Vineux, J., "Three-dimensional frequency-domain full waveform inversion with phase encoding," in [*SEG Technical Program Expanded Abstracts 2009*], 2288–2292, Society of Exploration Geophysicists (2009).
[29] Warner, M., Stekl, I., and Umpleby, A., "Full wavefield seismic tomography–iterative forward modelling in 3d," in [*69th EAGE Conference and Exhibition incorporating SPE EUROPEC 2007*], (2007).
[30] Wright, S. and Nocedal, J., "Numerical optimization," *Springer Science* **35**, 67–68 (1999).
[31] Virieux, J. and Operto, S., "An overview of full-waveform inversion in exploration geophysics," *Geophysics* **74**(6), WCC1–WCC26 (2009).
[32] Abràmoff, M. D., Magalhães, P. J., and Ram, S. J., "Image processing with imagej," *Biophotonics international* **11**(7), 36–42 (2004).
[33] Guide, M. U., "The mathworks," *Inc., Natick, MA* **5**, 333 (1998).
[34] Chen, Z., Cheng, D., Feng, W., and Wu, T., "An optimal 9-point finite difference scheme for the helmholtz equation with pml," *Int. J. Numer. Anal. Model* **10**, 389–410 (2013).